Shoaling of abyssal ventilation in the Eastern Indian Sector of the Southern Ocean

Keishi Shimada[1*], Yujiro Kitade[2], Shigeru Aoki[3], Kohei Mizobata[2], Lingqiao Cheng[4, 5], Kunio T. Takahashi[6, 7], Ryosuke Makabe[2, 6, 7], Jota Kanda[2, 6], Tsuneo Odate[6, 7**]

[1] Centre for Marine Research and Operations, Tokyo University of Marine Science and Technology, 4-5-7, Kounan, Minato-ku, Tokyo, 108-8477, Japan.

[2] Department of Ocean Sciences, Tokyo University of Marine Science and Technology, 4-5-7, Kounan, Minato-ku, Tokyo, 108-8477, Japan.

[3] Institute of Low Temperature Science, Hokkaido University, Kita-19, Nishi-8, Kita-ku, Sapporo, 060-0819, Japan.

[4] College of Marine Sciences, Shanghai Ocean University, No. 999, Huchenghuan Rd., Lingang Special Area, Shanghai 201306, China.

[5] Centre for Polar Research, Shanghai Ocean University, No. 999, Huchenghuan Rd., Lingang Special Area, Shanghai 201306, China.

[6] National Institute of Polar Research, Research Organization of Information and Systems,10–3 Midori-cho, Tachikawa, Tokyo 190-8518, Japan.

[7] Department of Polar Science, The Graduate University for Advanced Studies (SOKENDAI), 10–3 Midori-cho, Tachikawa, Tokyo, 190–8518, Japan.

*Email: kshima0@kaiyodai.ac.jp

** Deceased.

Supplementary Information:

Supplementary Note S1. Details on the hydrographic data (Figure S1; Table S1)

In this study, we used data observed along the WOCE/GO-SHIP section I08s, I09s and SR3, which span from the AAB to SAB (Fig. S1). Also, the core AAB is repeatedly observed in summer of the year from 2011 to 2019 by training and research vessel Umitaka-Maru of Tokyo University of Marine Science and Technology (Fig. 1a). Here we describe details of these data (details are also summarized in Table S1).

At each WOCE/GO-SHIP section, summer hydrographic data were repeatedly observed from 1990s to 2010s and these data are available online at https://cchdo.ucsd.edu/. Umitaka-Maru repeatedly conducted Summer hydrographic observations in the offshore region between the Vincennes Bay and Sabrina coast. High-quality top-to-bottom profiles of temperature and salinity were collected using a Seabird 911 conductivity-temperature-depth (CTD) profiler. For DO profiles, the JFE Alec Rinko Optode was used after 2015, and the Seabird SBE-43 was used prior. As described in previous studies[1, 2], the methodologies for data processing, water sampling, measurements, and data calibration followed the recommendations for the instruments and methods of the Global Ocean Ship-Based Hydrographic Investigation Program (GO-SHIP)[3] to the greatest extent possible. As a result, the accuracy of the salinity and temperature measurements were expected to fall within the World Ocean Circulation Experiment (WOCE) targets of 0.002 °C and 0.002 PSS-78, respectively[4]. For DO data calibration, which is not described in previous studies[1, 2], we followed the procedure outlined in Hood et al. [3], such that the accuracy was expected to remain within the WOCE target range.

Salinity correction requires some discussion. The International Association for the Physical Sciences of the Oceans (IAPSO) Standard Seawater (SSW) used for salinity correction is known to have salinity offsets which depend on batch number. We thus applied the salinity offsets as far as possible. Batch-to-batch offsets are from Kawano et al. [5] and Uchida et al. [6] and summarized in table S1. They ranged from -0.6×10^{-3} to 0.7×10^{-3} PSS-78. Regarding data obtained by Umitaka-Maru in 2011 and 2012, however, SSW offsets could not be applied because SSW batch number was not available. Purkey and Johnson[7] further applied additional ad hoc salinity adjustments which is based on the θ–S comparison in geographical regions containing water that has been isolated from the surface for a relatively long time. However, we did not apply this adjustment because we consider possibility that ventilation is reaching circumpolar deep water; which was assumed to be the oldest water that in the Southern Ocean.

Supplementary Note S2. Data selection and gridding along sections (Figures S2, and S3).

S2a. Data selection and applicability for multi-decadal variability estimation

To obtain a multi-decadal time series in the core Australian-Antarctic Basin (AAB), data were mapped to combine the results from multiple sections. Prior to this mapping, the applicability of combining data observed at these sections together was assessed. During the assessment, bottom depth, particularly considering the along-isobath flow that forms under a strong Coriolis effect and weak stratification[8], and spatial difference among the core-AAB were considered.

After 2011, the training and research vessel Umitaka-Maru obtained summer hydrographic data in the offshore region between the Vincennes Bay and Sabrina coast (Fig. 1a). While the horizontal resolution at I09s was maintained constant at ~30', it differed considerably at 110° E depending on the bottom depth and latitude (Supplementary Note S1 provides details of hydrographic data used in this study). The horizontal resolution along 110° E and 115° E was higher than 60' for much of the lower- to mid-slope region (4,500–2,200 m bottom depth) throughout most of the year. Thus, horizontal resolution among Umitaka-Maru and WOCE/GO-SHIP sections remained relatively comparable using data that meet the bottom depth range. However, especially in shallower southern region, meridional extent of the sections is influenced by sea ice extension, which presents inter-annual fluctuations. Thus, the shallower limit was modified to 2,600 m to avoid being influenced by sea ice extension in the gridding procedure, the product of which was used for quantitative analysis such as the sea-level rise (SLR). We then confirmed the spatial differences among the core AAB. Fortunately, data were obtained almost simultaneously (within three weeks) in January 2012 at 110° E and the slightly shifted I09s owing to sea ice. The θ–S curves of both sections were in good agreement (Fig. S2a), and isopycnal salinity differences (Fig. S2b) were generally within the WOCE accuracy requirements for salinity (0.002 PSS-78)[4] in the layer below the isopycnal of $\gamma^n = 28.1$ kg m^{-3} (~950 m). Thus, we concluded that the spatial differences among the study areas were negligible and that the combined data were applicable for the estimation of the multi-decadal variability. (Note that, in the above procedure determining the difference between the section, data obtained from shallower region than 3,000 m was not used to avoid being influence by highly variable or transient signals derived from the continental shelf).

S2b. Gridding along sections and reference data for 1995

Quantitative assessments from data observed at different sections were conducted by interpolating both conditions in 1995 and the data observed at each section onto the same horizontal and vertical grids. Figure S3 shows the horizontal grid points spaced 10 km along each section. Vertical grid points ranged from the surface (0 m) to the bottom, with a spacing of 1 m. The conditions in 1995 are given for each grid by interpolating the WOCE/GO-SHIP I09s data observed in 1995 (shown in Fig. S3 by yellow circles) with the Topographic Constraint-Incorporated scheme and decorrelation scales[9]. The data observed at each section were interpolated using the same scheme and decorrelation scales. For surface data, we extrapolated the shallowest data in the observed vertical profile to the surface if data above 10 m were obtained.

Supplementary Note S3. Effect of meridional shift in Southern Antarctic Circumpolar Current Front on observed long term trends (Figures S4, S5, and S6)

In this section, the causes of observed temperature and salinity changes are discussed based on their patterns. The temperature change was compared with the change in the position of the SACCF, i.e., the southern limit position where the local temperature maximum exceeded 1.8 °C[10]. This temperature criterion was chosen because its southern limit in climatological data (shown as a green line in Fig. 1a) was roughly centred within the study area; thus, the determined change is expected to represent the variability in the study area. Practically, the position is expressed as the bottom depth where it is located, allowing changes in the position to be expressed consistently among different sections.

The isobaric temperature change had a high negative correlation (correlation coefficient < –0.58) with the SACCF depth anomaly (anomaly at the bottom depth of the southern limit of 1.8 °C) throughout the layers below the temperature maximum (~400 m; Fig. S4a). Thus, the overall temperature change was highly barotropic and SACCF dependent. The steric SLR and SACCF depth anomalies were compared in the time-series (Fig. S5). The SACCF depth shoaled throughout the observation period (–87 ± 48 m decade^{-1} or –218±120 m during observed period spanning 25 years), such that the SACCF shifted toward the south (22 ± 12 km decade^{-1} or 55±30 km during the observed period spanning 25 years). (Please note that SACCF depth anomaly was converted to a meridional positional anomaly using the average topographic gradient in the core AAB). Thermosteric SLR had a high negative correlation with the SACCF anomaly, in both the deep (correlation coefficient: –0.73) and shallow layers (correlation coefficient: –0.80), which increased throughout the observation period (Fig. S5a, b). Together with the positive meridional temperature gradient (the axis is taken as positive in the northward direction; see Figs. S4b and S6a), high negative correlation suggest that the majority of the observed warming was induced by the southward shift in the SACCF.

Furthermore, the vertical profiles of the multi-decadal trends and meridional temperature gradients (Fig. S4b and c) were similar. Namely, they exhibit a maximum in the mid to deep layers (1,000–3,000 m), which decreased toward the bottom (correlation coefficient below 400 m is 0.71). This similarity may reflect a barotropic southward shift in the SACCF, because this process would induce warming proportional to the meridional gradient. Further, this assumption is quantitatively supported as the required southward shift to induce the observed warming (calculated based on the meridional temperature gradient; 29.2 km decade^{-1}) and southward shift directly estimated from the temperature distribution (22 ± 12 km decade^{-1}) were consistent. The meridional temperature gradient was obtained by averaging the horizontal gradients estimated for each section, whose temporal variability was small (see the standard deviation envelope in Fig. S4b). Additionally, when estimating the meridional gradients, only the horizontal gradients from grid points where the bottom depth exceeded 3,500 m were included to exclude the locally increased gradient near the continental shelf.

The cause of the southward shift in the SACCF in the AAB and whether this phenomenon occurred throughout the Southern Ocean are not entirely clear. However, the Antarctic Oscillation (AAO) index (monthly mean AAO index data provided by the National Oceanographic and Atmospheric Administration was used), which was smoothed by a two-year moving average (shown by the grey triangles and dashed lines in Fig. S5), was highly correlated with the SACCF depth anomaly (correlation coefficient of –0.72) and deep and shallow thermosteric SLR, with correlation coefficients of 0.80 and 0.66, respectively (Fig. S5a, b). A high correlation was also confirmed for isobaric temperature changes below the salinity maximum layer (Fig. S4a). Thus, it is likely that the SACCF position and the induced warming responded to the large-scale atmospheric variability.

In contrast, the sign of the salinity change (freshening) and the meridional salinity gradient (salinity increases to the north; Fig S6b) in the layers below 1,600 m were opposite (Figs. S4e, f); hence, freshening in those layers cannot be explained by the southward shift in the SACCF. The halosteric SLR in both the deep and shallow layers was uncorrelated with both the SACCF depth anomalies and AAO index values (Fig. S5c, d). These results indicate that the cause of the observed freshening was not the southward shift in the SACCF, but rather by freshening in the source regions and waters.

Supplementary Note S4. Division of steric SLR into frontal shift and water-mass change components

Based on the division of observed warming and freshening into the water mass change and SACCF shift component, the steric SLR was decomposed into two components. Throughout the water column, the water mass change component (1.4 ± 1.8 mm y^{-1}) accounted for 54 % of the observed steric SLR (2.7 ± 1.6 mm y^{-1}). The deep-layer contribution (1.1 ± 0.6 mm y^{-1}) was important, whereas the deep halosteric component (0.7 ± 0.2 mm y^{-1}) dominated the signal. Regarding the SACCF shift components, which accounted for the remaining 46 %, thermosteric component (1.2 ± 0.6 mm y^{-1}) of the deep (0.6 ± 0.3 mm y^{-1}) and shallow (0.6 ± 0.3 mm y^{-1}) layers explained almost all because the halosteric components of the layers above and below the salinity maximum compensated for each other. Thus, the water mass change and meridional shift contributed almost equally to SLR throughout the water column, although the impact of the water mass change was largely confined to the deep layer.

Supplementary Note S5. Spatial representativeness of trends obtained along WOCE/GO-SHIP I09s and in the core AAB for the SAB and AAB (Figure S7)

To confirm the spatial representativeness of the multi-decadal trends obtained along WOCE/GO-SHIP I09s and in the core AAB for the SAB and AAB, respectively, they were compared with those estimated using all of the data observed along the three WOCE/GO-SHIP sections SR3, I09s, and I08s. At each section, summer observations were conducted three times. After interpolating the data observed at each section onto the same horizontal and vertical grids in the manner described in section S2b, the multi-decadal trends with their errors (95 % confidence interval) were estimated for the respective basins following previously described methodologies[11].

For the SAB, the estimated trends and errors using three sections (Fig. S7a and b) and those using only I09s (Figs. 5d and e or S7c and d) were consistent; thus, the trends obtained along I09s successfully represented the SAB. We also discuss the effect of the southward shift in the ACC on the estimated trends. The southward shift in the SACCF in the core AAB was confirmed from both the hydrography (e.g., Fig. S5) and satellite altimetry[12,13]. In the SAB, however, the south ward shift was not clear in both the hydrography (not shown) and satellite altimetry[12,13]. Thus, the effect of the southward shift in the ACC on estimated trends in the SAB was expected to be smaller than that in the core AAB.

Testing representativeness of multi-decadal trends obtained in the core AAB is difficult owing to the evident southward shift in the ACC. While the effect of the southward shift was removed in the water mass changes obtained in the core AAB, it was difficult to remove them from the trends estimated for the entire AAB. This is because that clear relation between meridional shift of ACC and observed variation (e.g., correlation coefficient between temperature variation and SACCF position; fig. S4a) was not found for observations along the WOCE/GO-SHIP section which are repeated only three times. Even though, reduced warming and AOU decreasing tendency in less dense LMOC likely represent whole the basin because they were confirmable in both trends (Fig. S7e-h).

Supplementary Note S6. Increasing intrusion in the less dense LMOC (Figures S8 and S9)

Intrusions of cool, fresh, and oxygen-rich water were frequently observed in the layers below the salinity maximum. The vertical scale of intrusions ranged from a few tens to hundreds of metres; intrusions locally induce fresh, cool, and oxygen-rich anomalies (Fig. S8a, b). Induced negative salinity anomalies, which were frequently observed in recent observations after 2012, widely distributed vertically (Fig. S9a–d). The estimated salinity anomalies were converted to the required freshwater input (Fig. S9e–h); the total freshwater input was largest in 2015 while freshening was most evident throughout the time-series (Fig. 2a).

Here, only the sections with a horizontal resolution of 30’ or higher at the lower to mid-slope (i.e., bottom depth shallower than 4,000 m), where intrusion signals were frequently observed, were selected. We note, however, that detected anomalies were generally not continuous along the isopycnal even at a higher horizontal resolution above 30’ (Fig. S9i), implying that the horizontal scale of intrusion was smaller than 30’. While the increasing trend in the intrusions was clear, the estimated freshwater inputs (Fig. S9e–h) may be under or overestimated due to spatial aliasing.

The methods used to determine the intrusion and induced anomalies are described below. In the layers below the salinity maximum, the water column is stratified so that warm and saline water overlies cool and freshwater. In this case, the Turner angle (*Tu*)[14] has a value between 45° and 90° (Fig. S8c). The intrusion of cool and fresher water into the layer with an identical density forms a different stratification from that of the background. In other words, near the upper boundary, stratification would be warm and saline toward the upper layer (45 < *Tu* < 90°), but closer to the density compensation (*Tu* of ~90°) than in the background. Near the lower boundary, stratification would be cool and fresh toward the upper layer (–90 < *Tu* < −45°). Hence, *Tu* values below –45° and above the third quartile (Fig. S8c) were used to determine the intrusions. First, the *Tu* minimum, with a value < –45° (blue circle in Fig. S8a), and

Tu maximum, with values above the third quartile (red circle in Fig. S8a), located above the minimum, were paired. Then, the lower boundary of the intrusion was defined as the first layer in which *Tu* has a value above –45° in the layers below the *Tu* minimum (solid grey line in Fig. S8a), whereas the upper boundary was defined as the first layer in which the *Tu* value was lower than the third quartile in the layers above the *Tu* maximum (broken grey line in Fig. S8a). Induced anomalies were estimated at each isobaric surface as the difference between the observed profiles (red, blue, and green solid lines in Fig. S8a) and linearly interpolated profiles between the upper and lower boundaries of the intrusions (red, blue, and green broken lines in Fig. S8a).

Supplementary Note S7. Water mass properties difference between the South Australian Basin and the Australian-Antarctic Basin (Figure S10)

By using WOCE/GO-SHIP I09s data obtained during 1995-2012, climatological water mass properties are estimated for the SAB and AAB, respectively (fig. S10). It is clear that AAB is fresher, cooler, and low AOU than the SAB on the isopycnal below γ^n = 28.02 kg m^{-3}.

Supplementary Note S8. Climatological distribution of height above the bottom and AOU of the less dense LMOC (Figure S11)

To confirm the pathway and source of the lower AOU water for the less dense LMOC, the height above the bottom and the AOU on the isopycnal at γ^n =28.10 kg m^{-3}, which is almost the mid-point density between the upper

(28.02 kg m^{-3}) and lower (28.19 kg m^{-3}) boundaries, was determined (Fig. S11) using the WOCE global ocean hydrographic data[15].

The less dense LMOC was confirmed to be widely distributed over the Southern Hemisphere (Fig. S11b) with less topographic interruption relative to the densest LMOC [16]. The SAB is mainly connected on the isopycnal with the AAB to the south, the Wharton basin (WB) to the northwest, and the Tasman Basin (TS) to the east. AOU in the AAB was the lowest among these basins (Fig. S11a); hence, it is reasonable to assume that a plausible oxygen source is the AAB.

References in Supplementary Information:

1. Shimada, K. Makabe, R. Takao, S. & Odate, T. Physical and chemical oceanographic data during Umitaka-maru cruise of the 58th Japanese Antarctic Research Expedition in January 2017. *Polar Data J.* **4,** 1-29 (2020).

2. Shimada, K. et al. Physical and chemical oceanographic data during Umitaka-maru cruise of the 59th Japanese Antarctic Research Expedition in January 2018, *Polar Data J*. **5,** 11-36 (2021).

3. Hood, E. Sabine, C. Sloyan, B. M. Eds., The GO-SHIP Repeat Hydrography Manual: A Collection of Expert Reports and Guidelines (IOCCP Report No. 14, ICPO Publication Series No. 134, International CLIVAR Project Office, 2010). Available online at http://www.go-ship.org/HydroMan.html

4. Joyce, T. M. in *WHP Operations and Methods, WOCE Operations Manual* (WHP Office Report, WHPO 91-1, WOCE Report No. 68/91, Woods Hole Oceanographic Institution, Woods Hole, MA, 1994), 1-4 pp.

5. Kawano, T. et al. The latest batch-to-batch difference table of Standard Seawater and its application to the WOCE onetime sections, *J. Oceanogr.*, **62**, 777–792 (2006).

6. Uchida, H. et al. An Expanded Batch-to-Batch Correction for IAPSO Standard Seawater. *J. Atmos. Ocean. Technol.* **37**, 1507-1520; 10.1175/JTECH-D-19-0184.1 (2020).

7. Purkey, S. G. & Johnson, G. C. Antarctic Bottom Water warming and freshening: Contributions to sea level rise, ocean freshwater budgets, and global heat gain. *J. Clim.* **26**, 6105-6122; 10.1175/JCLI-D-12-00834.1 (2013).

8. Pedlosky, J. *Geophysical Fluid Dynamics* (Springer, New York, ed. 2, 1987).

9. Shimada, K., Aoki, S. & Ohshima, K. I. Creation of a gridded dataset for the Southern Ocean with a topographic constraint scheme. *J. Atmos. Ocean. Technol.* **34**, 511-532; 10.1175/JTECH-D-16-0075.1 (2017).

10. Orsi, A. H., Whitworth, T. & Nowlin, W. D. On the meridional extent and fronts of the Antarctic Circumpolar Current. *Deep Sea Res. I* **42**, 641-673; 10.1016/0967-0637(95)00021-W (1995).

11. Purkey, S. G. & Johnson, G. C. Warming of global abyssal and deep Southern Ocean Waters between the 1990s and 2000s: Contributions to global heat and sea level rise budgets. *J. Clim.* **23**, 6336-6351; 10.1175/2010JCLI3682.1 (2010).

12. Kim, Y. & Orsi, A. H. On the variability of Antarctic Circumpolar Current fronts inferred from 1992-2011 altimetry. *J. Phys. Oceanogr*. **44,** 3054-3071 (2014).

13. Sokolov, S. & Rintoul, S. R. Circumpolar structure and distribution of the Antarctic Circumpolar Current fronts: 2. Variability and relationship to sea surface height. *J. Geophys. Res.*, **114,** (2009).

14. Ruddick, B. R. A practical indicator of the stability of the water column to double-diffusive activity, *Deep-Sea Res.,* **26,** 903-913 (1983).

15. Gouretski, V.V. & Koltermann, K.P. WOCE global hydrographic climatology. Berichte des Bundesamtes für Seeschifffahrt und Hydrographie Rep. **35,** 52 pp (2004).

16. Orsi, A. H., Johnson, G. C. & Bullister, J. L. Circulation, mixing, and production of Antarctic Bottom Water. *Prog. Oceanogr.* **43**, 55-109; 10.1016/S0079-6611(99)00004-X (1999).

Figures in Supplementary Information:

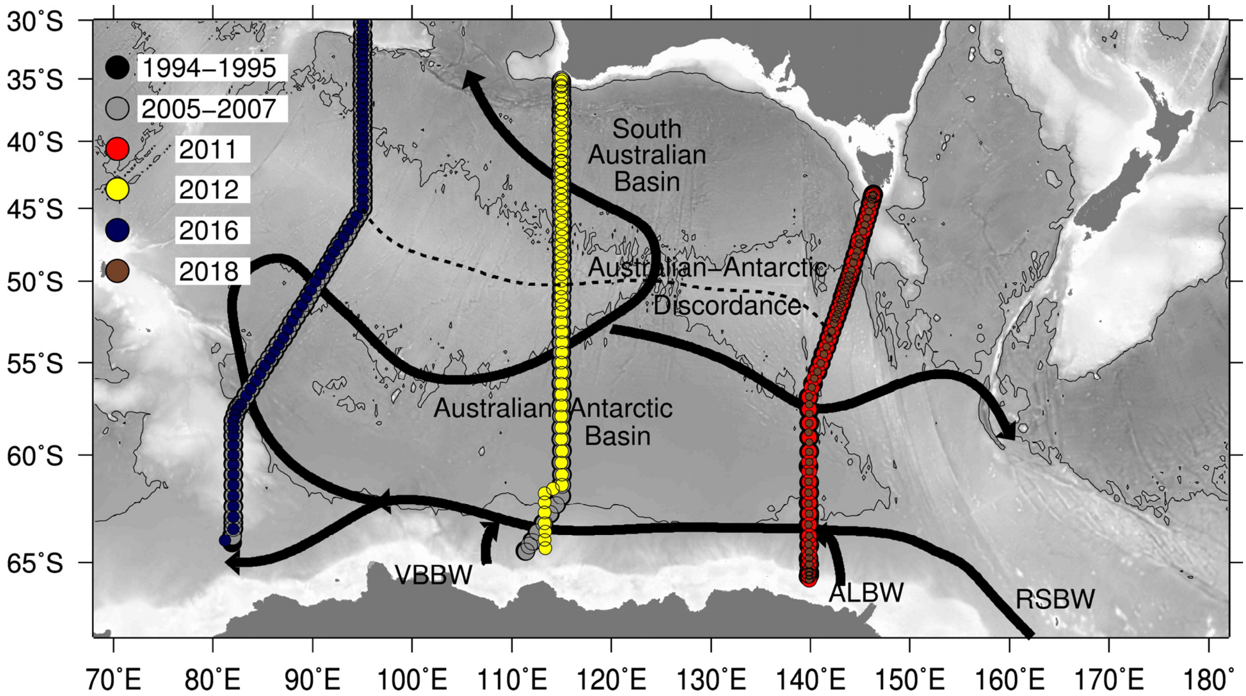

Figure S1. Distribution of the WOCE/GO-SHIP data used for the multi-decadal trends in the South Australian Basin (SAB) and Australian Antarctic Basin (AAB)

The distribution of the data obtained along WOCE/GO-SHIP sections SR3, I09s, and I08s in the SAB and AAB is shown. The broken black line indicates the boundary between the basins, determined as the shallowest portion of the Southeast Indian Ridge. The observation points are coloured according to the observation year. The thin solid black line indicates the 4,000 m isobath. Black arrows indicate the Antarctic Bottom Water (AABW) pathways, and the major AABW supply (ALBW, VBBW, and RSBW) are the same as those given in Fig. 1a.

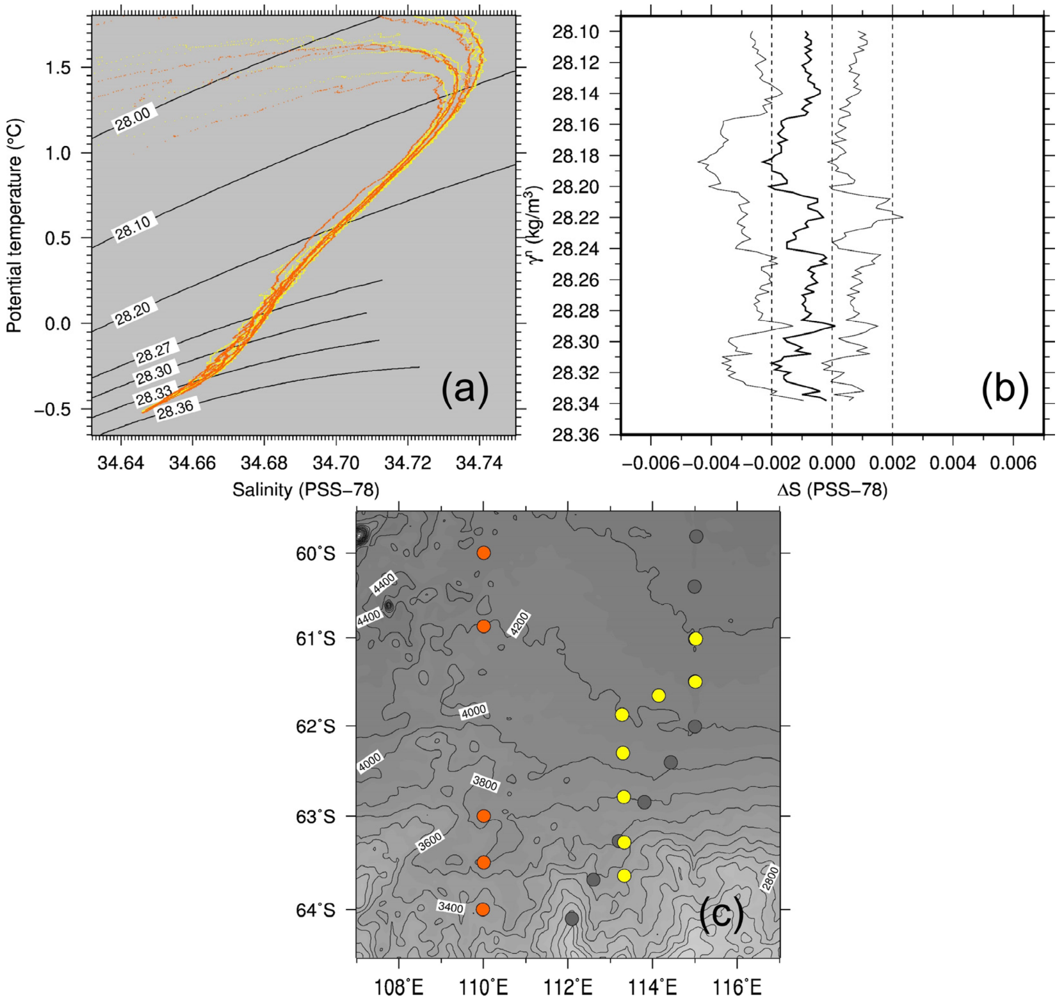

Figure S2. θ-*S* differences between 110° E and the I09s observed in January 2012

(**a**) θ-S diagram for 110° E and the slightly shift I09s owing to sea ice. (**b**) Isopycnal salinity differences between 110° E and the I09s. (**c**) Observation locations. Observations along 110° E and the I09s are indicated by orange and yellow dots, respectively, in (**a**) and (**c**). In (**b**), isopycnal differences are indicated by thick solid lines, with thin solid lines indicating standard deviations. Dashed lines in (**b**) indicate the WOCE requirement for salinity accuracy (0.002 PSS-78; *18*).

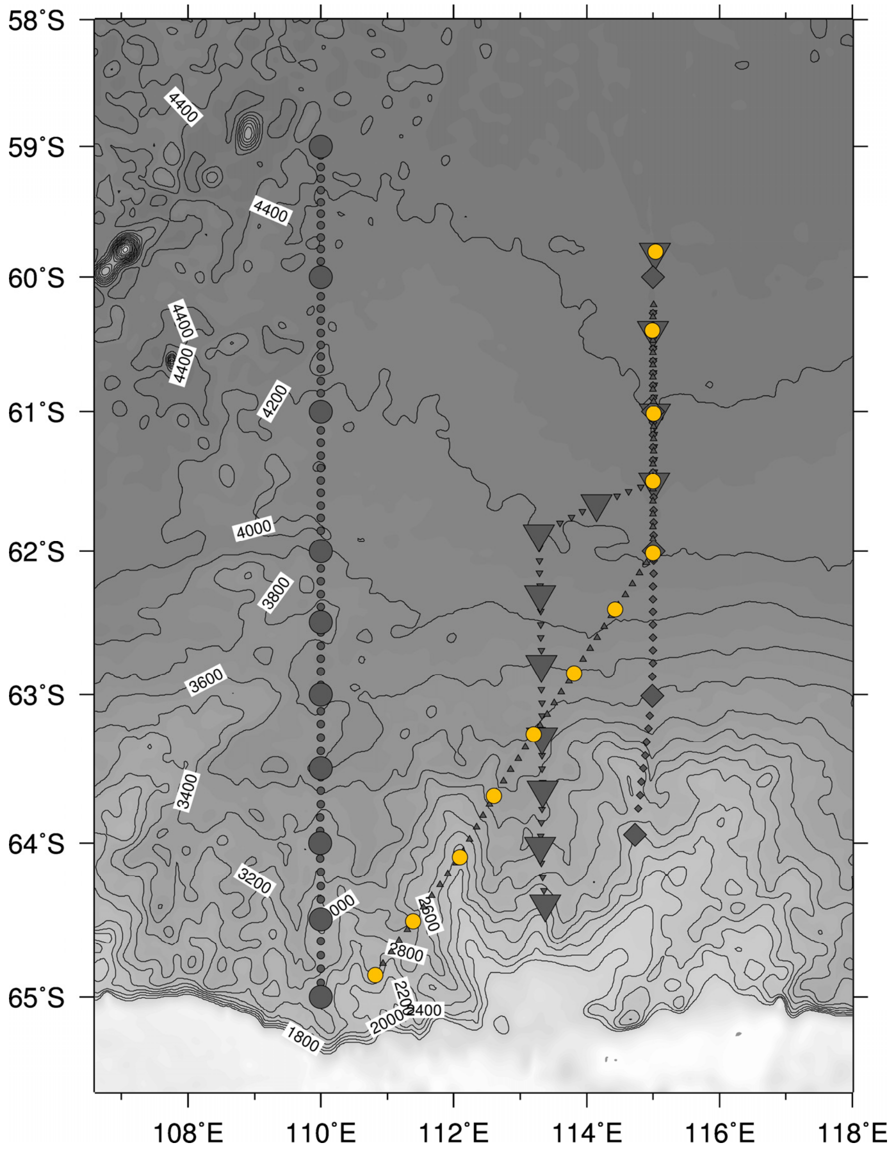

Figure S3. Position of the grids along each section and WOCE/GO-SHIP I09s data observed in 1995

Typical observation points along sections 110° E, WOCE/GO-SHIP I09s, slightly shifted I09s owing to sea ice, and 115° E are shown by large grey circles, small yellow circles, large grey inverted triangles, and large grey diamonds, respectively. Grid points along 110° E, I09s, slightly shifted I09s owing to sea ice, and 115° E shown by small grey circles, triangles, inverted triangles, and diamonds, respectively. The WOCE I09s data used to calculate the references for the conditions in 1995 are indicated by yellow circles

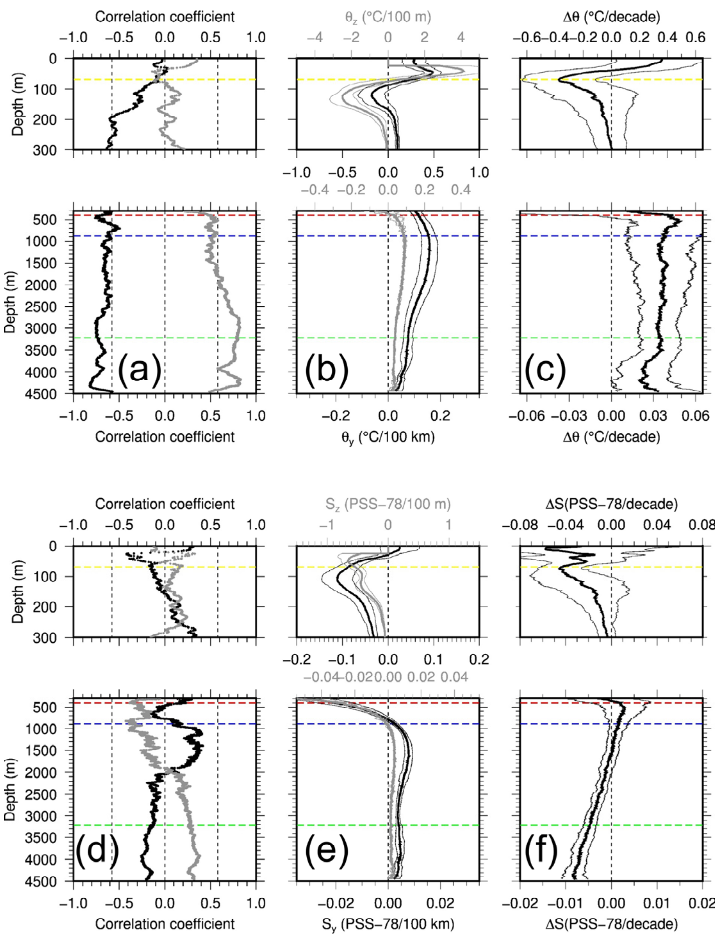

Figure S4. Vertical profiles of the correlation coefficients for isobaric temperature/salinity changes with the SACCF depth anomalies and AAO index values, along with a comparison between the multi-decadal trends and meridional/vertical gradients

Upper panels (**a**, **b**, and **c**) present variables derived from the potential temperature and lower panels (**d**, **e**, and **f**) present variables derived from the salinity. Left panels (**a** and **d**) indicate the correlation coefficients for the isobaric temperature and salinity change with the SACCF depth anomalies (black) and AAO index values smoothed by the two-year moving average (grey). The middle panels (**b** and **e**) indicate the meridional (black) and vertical (grey) gradients, respectively. Thin lines indicate standard deviations. The right panels (**c** and **f**) show the multi-decadal trends. Thin lines indicate the 95 % confidence interval. Each panel was divided into layers above and below 300 m.

The dashed yellow, red, blue, and green lines are defined in Fig. 2. Black dashed lines located at position of correlation coefficient -0.58 and 0.58 in (**a**) and (**d**) indicate 95% significance level for the correlation.

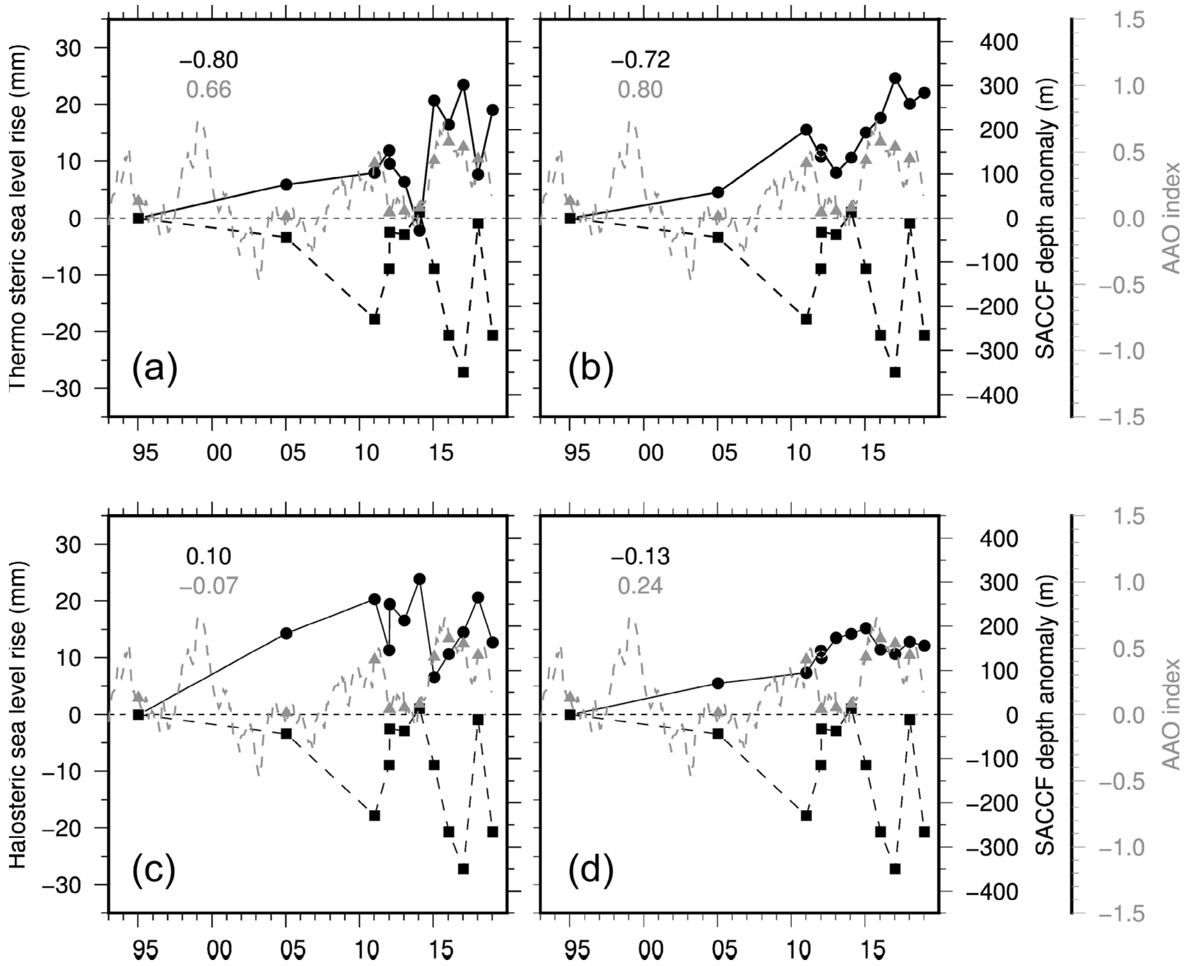

Figure S5. Time-series of the decomposed components of the steric SLR

Time-series of the thermo- (**a, b**) and halosteric (**c, d**) components: the left (**a, c**) and right (**b, d**) panels indicate the shallow and deep layer components, respectively. The steric SLR, Southern Antarctic Circumpolar Circular Front (SACCF) depth anomaly, and Antarctic Oscillation (AAO) index smoothed by the two-year moving average are shown by black circles with solid lines, black squares with dashed lines, and grey triangles with dashed lines, respectively. The numbers given in the top left of each panel indicate the correlation coefficients of the steric SLR with the SACCF depth anomalies (black) and AAO index values (grey). Two points are plotted for 2012, reflecting observations along a section at 110° E and the I09s.

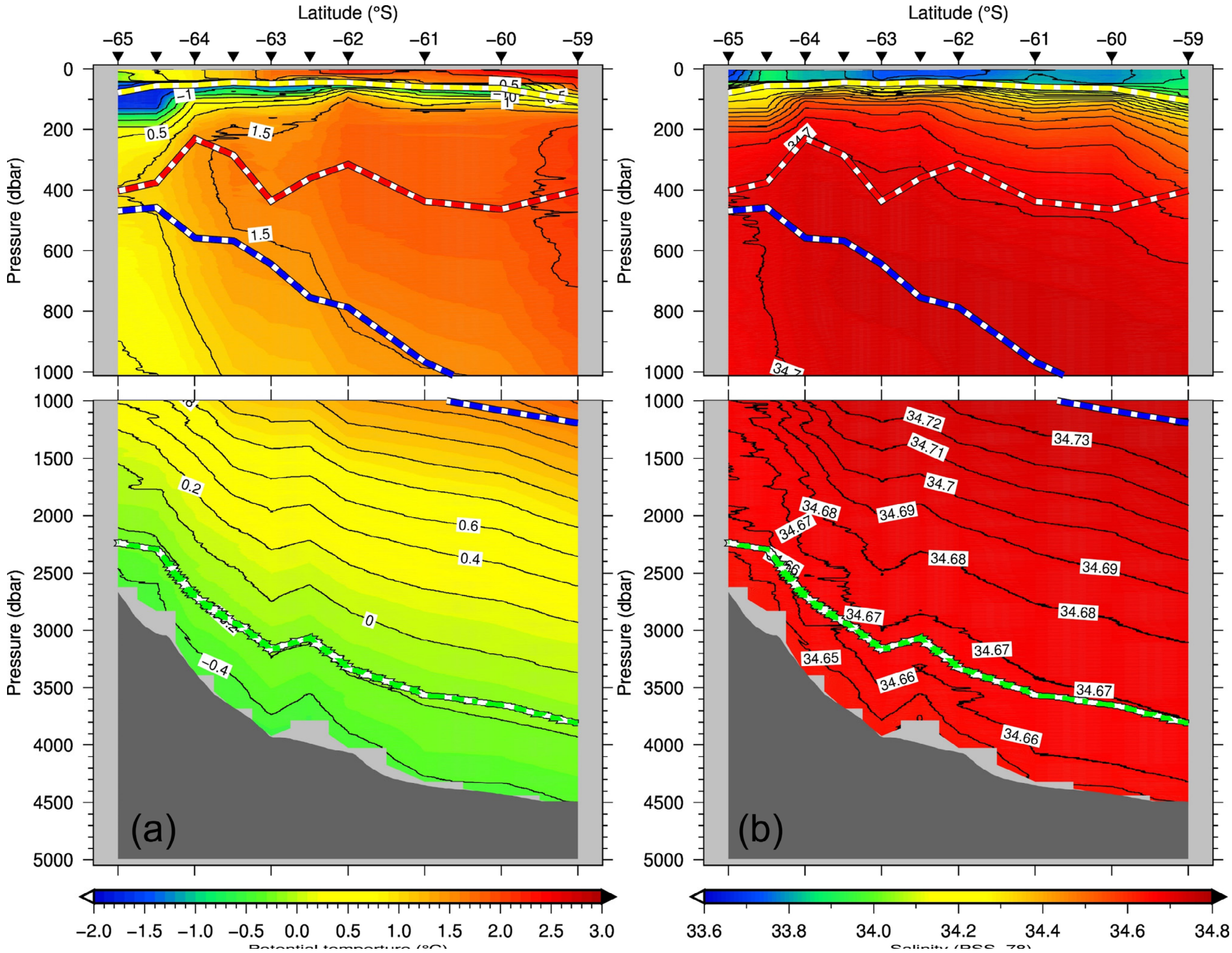

Figure S6. Meridional potential temperature and salinity along the 110° E section that obtained in 2015

(a) and (**b)** indicate the potential temperature and salinity, respectively. In both panels, the depths of the potential temperature minimum, potential temperature maximum, salinity maximum, and γ^n = 28.30 kg m^{-3} (corresponding to the top layer of the Antarctic Bottom Water) are shown by dashed yellow, red, blue, and green lines, respectively. The inverted triangles in both panels indicate the observed data points.

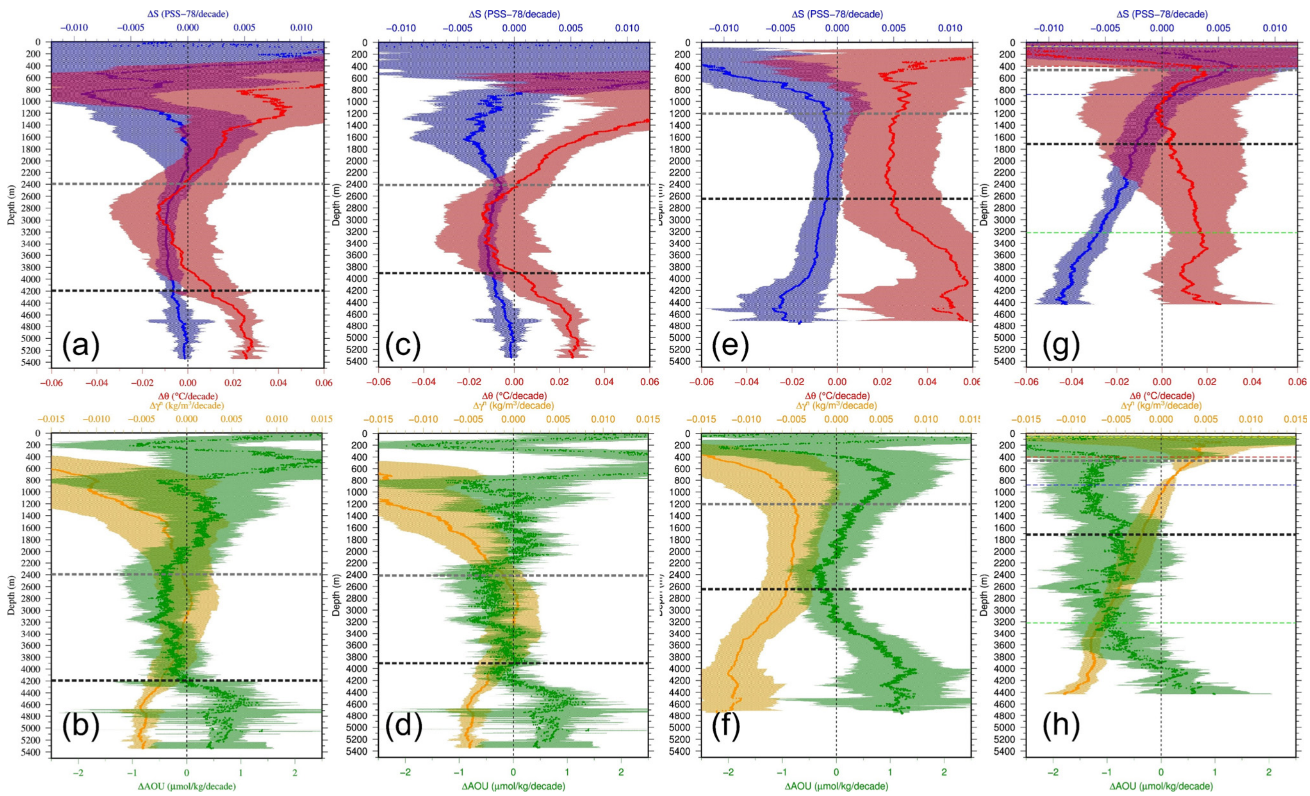

Figure S7. Vertical profiles of the multi-decadal trends in potential temperature, salinity, AOU, and neutral density in the South Australian Basin and the Australian-Antarctic Basin

Upper panels (**a**, **c**, **e**, and **g**) are multi-decadal trends of potential temperature and salinity. Lower panels (**b**, **d**, **f**, and **h**) are multi-decadal trends of AOU, and neutral density. **a** and **b** are multi-decadal trends in the SAB estimated using all the data obtained along WOCE/GO-SHIP section SR3, I09s, and I08s. **c** and **d** are multi-decadal trends in the SAB estimated using only the data obtained along I09s. **e** and **f** are multi-decadal trends in the AAB estimated using all of the data obtained along the three sections. **g** and **h** are water mass changes in the core AAB. Shaded area in all the panels indicate 95 % confidence interval. Gray and black broken lines in (**a**) to (**h**) indicate the isopycnals at γ^n = 28.02 and 28.19 kg m^{-3}, respectively. The dashed yellow, red, blue, and green lines in (**h**) are defined in Fig. 2.

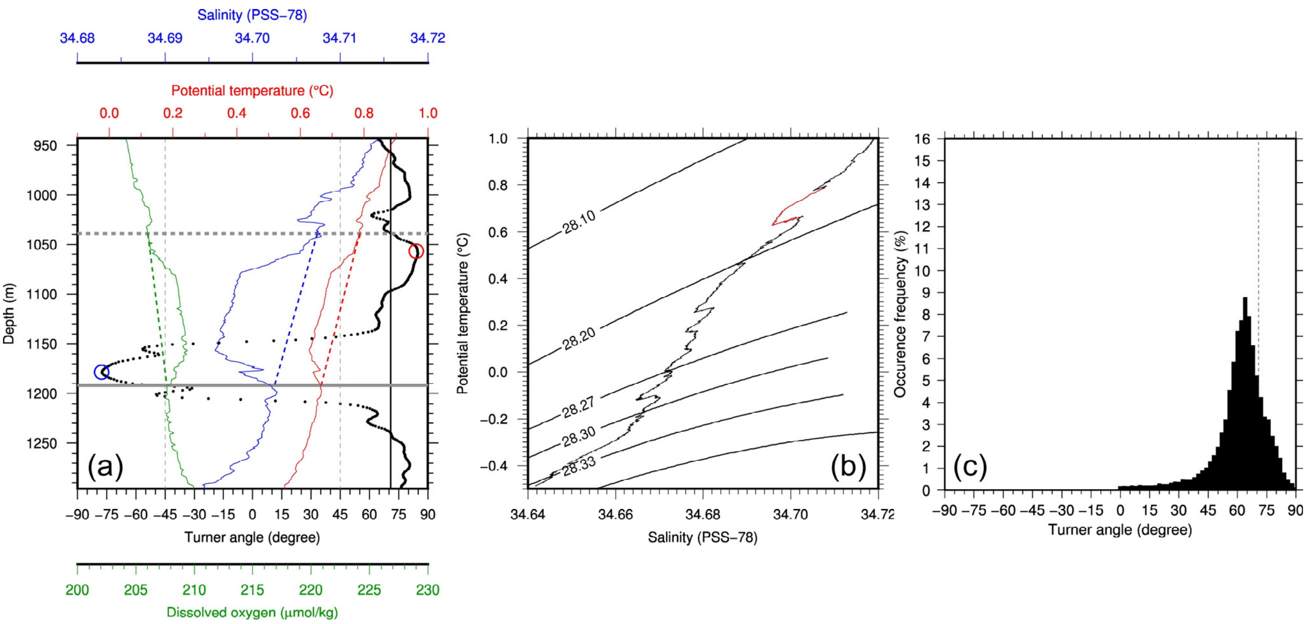

Figure S8. Example of the observed intrusion and definition of the induced anomaly

Observed intrusion exemplified from the observed data in 2015. (**a**) Vertical profiles of potential temperature (red), salinity (blue), DO (green), and Turner angle (*Tu*, black). The *Tu* minimum (below –45°) and maximum (above the third quartile) relevant to the determined intrusion are shown by blue and red circles, respectively. The lower and upper boundaries of the intrusion are shown by the grey solid and broken lines, respectively. (**b**) Determined intrusion in θ–S space. The background θ–S curve is shown by the black line, and that of the determined intrusion is highlighted in red. (**c**) Histogram of *Tu* in the layer below the salinity maximum determined using all of the data along 110° E obtained in 2015. The third quartile is shown by the broken grey line.

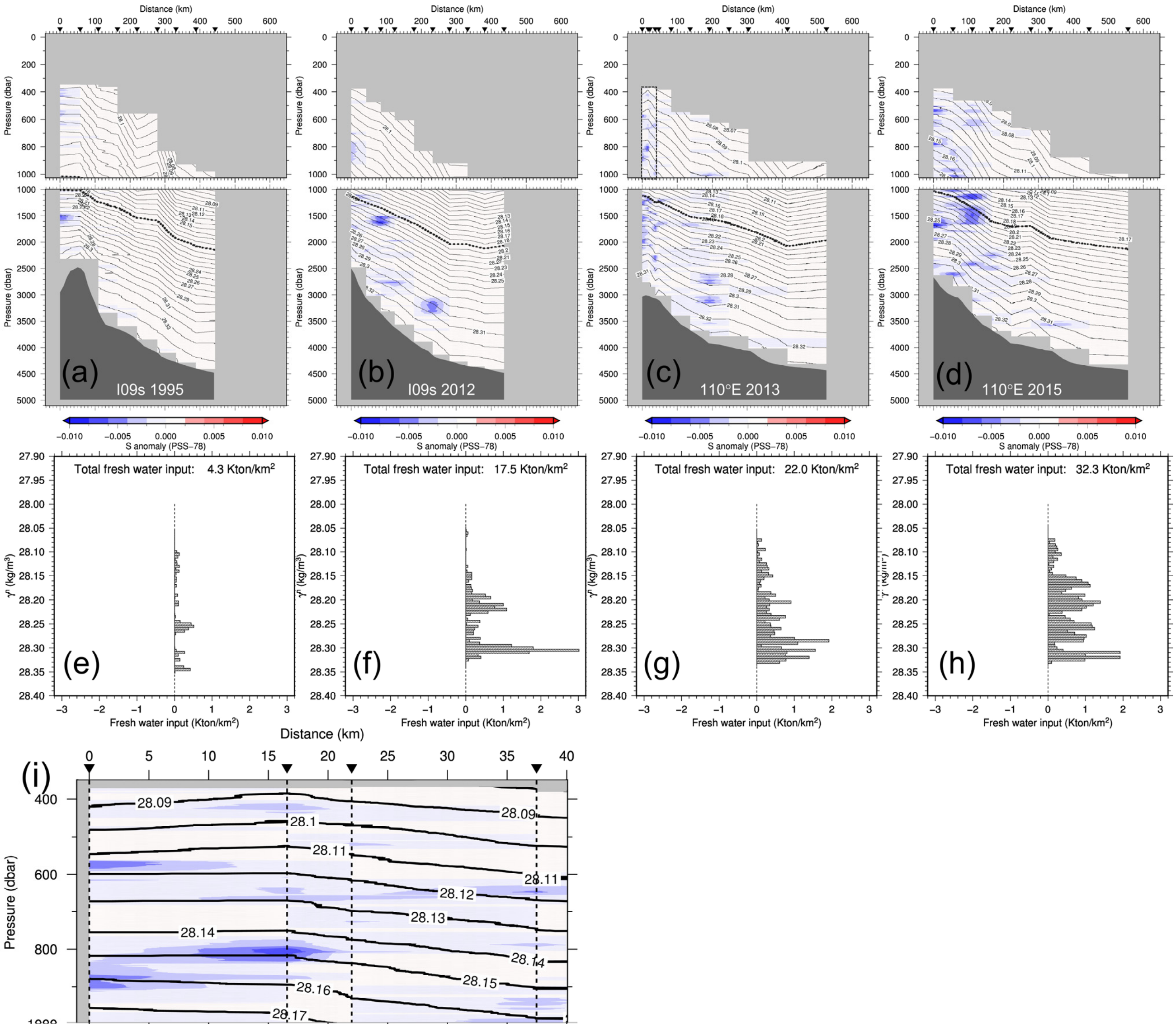

Figure S9. Salinity anomalies induced by the determined intrusion and required freshwater input

Upper panels (**a–d**) show the salinity anomalies induced by the determined intrusions along WOCE/GO-SHIP I09s, and 110° E observed in 1995, 2012, 2013, and 2015, respectively. The thick broken lines indicate the isopycnal at γ^n = 28.19 kg m^{-3}. The middle panels (**e-h**) show the required freshwater input for the determined intrusion as a function of γ^n. The lower panel (**i**) magnifies the area encompassed by the broken rectangle in (**c**). Broken lines indicate the location of the observations.

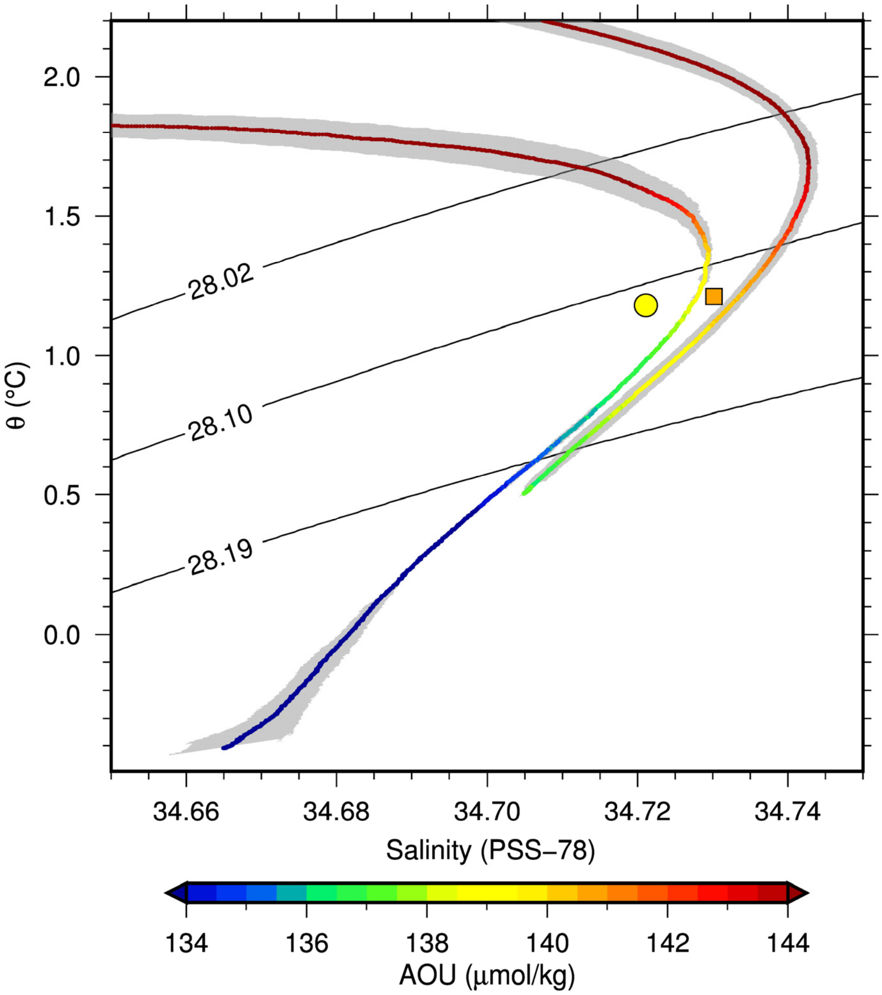

Figure S10. Water mass properties difference between the South Australian Basin and the Australian-Antarctic Basin

θ-S curves for the SAB (saltier curve on isopycnal) and AAB (fresher curve on isopycnal) are shown. θ-S curves are coloured according to AOU value. Gray shaded area indicate standard deviation estimated on isopycnals. Labelled contours indicate neutral density. Average θ, S, and AOU value of isopycnal between 28.02 and 28.19 are indicated by rectangle and circle for the SAB and AAB, respectively.

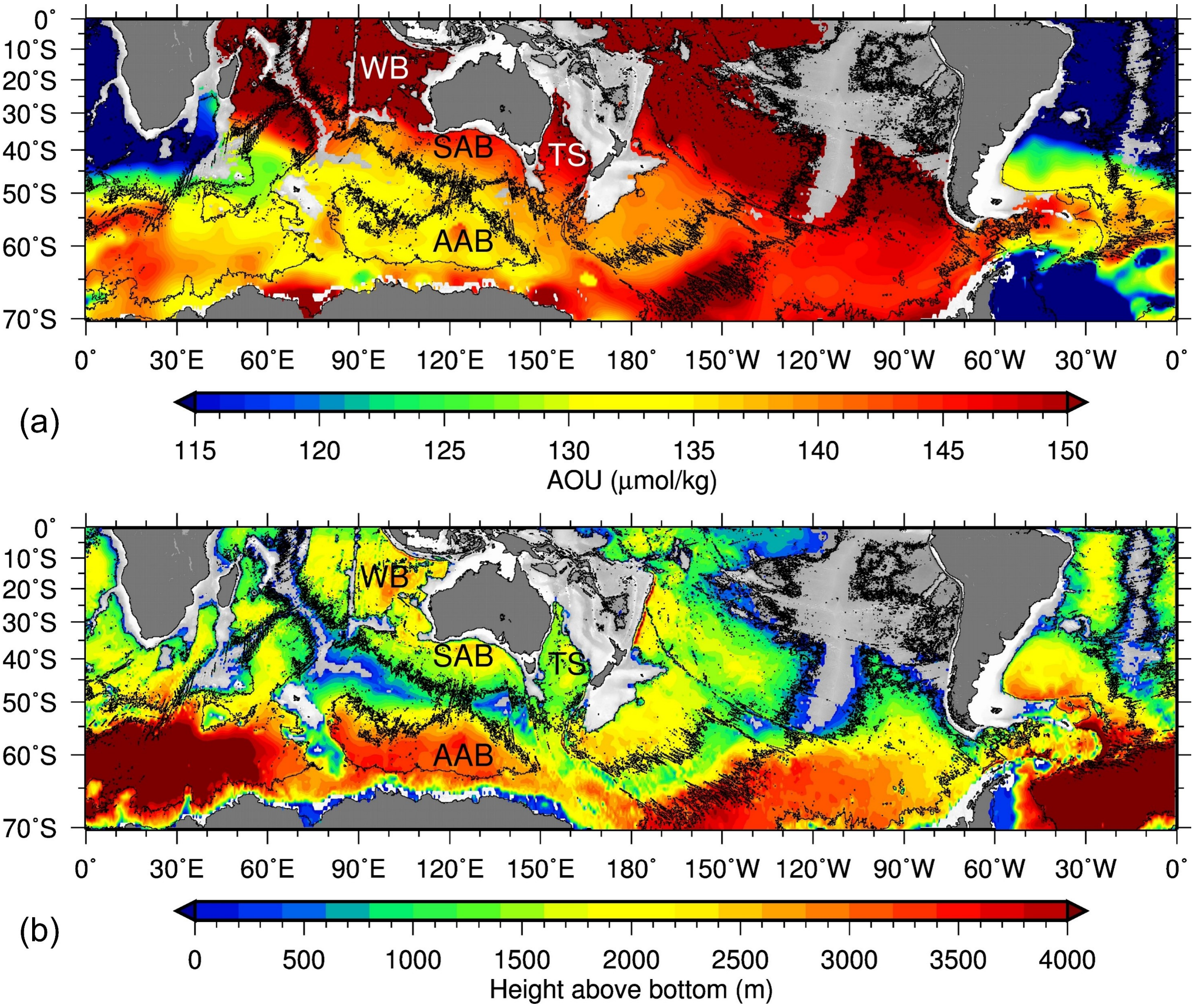

Figure S11. Climatological distributions of the height above the bottom and AOU of the less dense LMOC in the Southern Hemisphere

(**a**) Distribution of AOU on the less dense LMOC. (**b**) Height of the less dense LMOC above the bottom. The isopycnal at γ^n = 28.10 kg m^{-3}, which is almost the mid-point density between the upper (28.02 kg m^{-3}) and lower (28.19 kg m^{-3}) boundaries, was chosen to represent the less dense LMOC. The WOCE global Ocean hydrographic data[15] were used to derive (**a**) and (**b**). Thin black lines in (**a**) and (**b**) indicate the 4,000 m isobath. Related basins are labelled with abbreviations in (**a**) and (**b**): Australian-Antarctic Basin (AAB), South Australian Basin (SAB), Wharton basin (WB), and Tasman Sea (TS).

Tables in Supplementary Information:

Table S1. Summary of the CTD data used in this study

Observed year, month, WOCE/GO-SHIP section, latitude range, vertical resolution, SSW batch number, applied SSW offset[5, 6] were listed. For the I09s section, information for the core AAB (upper line) and whole the domain (lower line) is provided.

Year	Month	Section	Latitude range	Vertical resolution (dbar)	SSW batch number	SSW offset (×1000)
1994	12	I08s	64°8.8’S– 30°18.0’S	2	P 126	0.6
2007	2–3	I08s	63°52.8’S– 30°6.9’S	2	P147	-0.6
2016	2–3	I08s	64°3.0’S– 30°6.9’S	2	P158	-0.2
1995 1995	1 1	I09s	64°30.7’S– 59°48.2’S 64°30.7’S– 34°49.2’S	2	P124	0.6
2005 2004– 2005	1 12–1	I09s	64°31.3’S– 59°48.5’S 65°23.9’S– 34°49.2’S	2	P141	-0.3

2012 2012	1 1–2	I09s	64°24.1’S– 59°48.5’S 65°22.4’S– 34°27.4’S	2	P153	-0.4
1995	1–2	SR3	65°35.1’S– 43°59.9’S	2	P121/P123/P137/P140	0.4/0.7/-0.4/- 0.3
2011	1	SR3	65°42.8’S– 44°7.4’S	2	P149/150/151/152	0.7/0.7/-0.5/- 0.1
2018	1	SR3	65°42.7’S– 44°0.1’S	2	P161/158	-0.2/-0.2
2011	1	115° E	63°56.8’S– 60°0.0’S	1		
2012	1	110° E	64°56.8’S– 58°20.7’S	1		
2013	1	110° E	64°40.9’S– 59°1.4’S	1	P154	0.5
2014	1	110° E	65°0.0’S– 60°0.0’S	1	P156	0.4
2015	1	110° E	65°0.0’S– 59°0.0’S	1	P156	0.4
2016	1	110° E	64°58.5’S– 59°0.0’S	1	P158	-0.2
2017	1	110° E	65°17.0’S– 59°0.0’S	1	P158/P159	-0.2/-0.4

2018	1	110° E	64°40.4’S–59°0.0’S	1	P160	0
2019	1	110° E	65°0.5’S–59°0.0’S	1	P162	-0.5

Table S2. Total AOU changes and required changes in DSW supply

Total AOU changes and the required changes in DSW supply in the AAB, SAB, and the overall study area are given for the less dense LMOC and densest LMOC. Estimations in the AAB were provided for three patterns. For (a), estimations were derived using water mass changes obtained in the core AAB and for (b), they were derived from trends obtained along the three WOCE/GO-SHIP sections. For (c), averaged values of (a) and (b) are given.

a

	AAB	SAB	Study region total
Less dense LMOC	–8.72 ± 6.31 Tmol 0.51 ± 0.37 Sv	3.32 ± 5.08 Tmol 0.18 ± 0.28 Sv	–12.04 ± 11.39 Tmol 0.69 ± 0.65 Sv
Densest LMOC	0.53 ± 1.17 Tmol –0.05 ± 0.11 Sv	1.21 ± 1.97 Tmol –0.08 ± 0.12 Sv	1.74 ± 3.14 Tmol –0.13 ± 0.23 Sv

b

	AAB	SAB	Study region total
Less dense LMOC	1.33 ± 5.14 Tmol –0.08 ± 0.31 Sv	–3.32 ± 5.08 Tmol 0.18 ± 0.28 Sv	–1.99 ± 10.22 Tmol 0.11 ± 0.59 Sv
Densest LMOC	1.75 ± 1.62 Tmol –0.16 ± 0.14 Sv	1.21 ± 1.97 Tmol –0.08 ± 0.12 Sv	2.96 ± 3.59 Tmol –0.24 ± 0.26 Sv

c

	AAB	SAB	Study region total
Less dense LMOC	–3.70 ± 5.72 Tmol 0.22 ± 0.34 Sv	–3.32 ± 5.08 Tmol 0.18 ± 0.28 Sv	–7.02 ± 10.81 Tmol 0.40 ± 0.62 Sv
Densest LMOC	1.14 ± 1.40 Tmol –0.11 ± 0.13 Sv	1.21 ± 1.97 Tmol –0.08 ± 0.12 Sv	2.35 ± 3.37 Tmol –0.19 ± 0.25 Sv